

# CLUES about M33: the reversed radial stellar age gradient in the outskirts of Triangulum galaxy

Robert Mostoghiu<sup>1,2\*</sup>, Arianna Di Cintio<sup>2,3,4†</sup>, Alexander Knebe<sup>1,5,6</sup>,  
Noam I. Libeskind<sup>2</sup>, Ivan Minchev<sup>2</sup> & Chris Brook<sup>3,4</sup>

<sup>1</sup>*Departamento de Física Teórica, Módulo 15, Facultad de Ciencias, Universidad Autónoma de Madrid, E-28049 Madrid, Spain*

<sup>2</sup>*Leibniz-Institut für Astrophysik Potsdam (AIP), An der Sternwarte 16, D-144 Potsdam, Germany*

<sup>3</sup>*Instituto de Astrofísica de Canarias, Calle Vía Láctea s/n, E-38206 La Laguna, Tenerife, Spain*

<sup>4</sup>*Universidad de La Laguna. Avda. Astrofísico Fco. Sánchez, La Laguna, Tenerife, Spain*

<sup>5</sup>*Centro de Investigación Avanzada en Física Fundamental (CIAFF), Facultad de Ciencias, Universidad Autónoma de Madrid, 28049 Madrid, Spain*

<sup>6</sup>*International Centre for Radio Astronomy Research, University of Western Australia, 35 Stirling Highway, Crawley, Western Australia 6009, Australia*

Accepted XXX. Received YYY; in original form ZZZ

## ABSTRACT

HST/ACS observations along the major axis of M33 show that the mean age of its stars decreases with increasing distance from the galaxy center. Such a behavior is consistent with an inside-out growth of the disc. However, in the outermost observed field, at  $r \approx 11.6$  kpc, a reversal of this gradient is detected, with old stars found in high percentages beyond this radius. In this work we investigate the origin of such a reversal in stellar age gradient, by using a simulated M33 analogue from the Constrained Local Universe Simulations (CLUES). The simulated M33 is similar to the observed one in terms of mass, rotation velocity, surface brightness and, similar to what has been reported in observations, shows a stellar age turnaround at large radii. We demonstrate that this reversal is mostly a result of stellar accretion from old satellite galaxies and, to a lesser extent, of stellar migration of in-situ stars. The old accreted stars, with formation times  $t_f < 4$  Gyrs, are kinematically hot and can be differentiated from the in-situ stars by their high velocity dispersion and the fact that they do not have rotationally-supported orbits. In the future, obtaining kinematic information of the stars in the outskirts of M33 will help to verify this scenario.

**Key words:** methods:  $N$ -body simulations – galaxies: halos – galaxies: evolution – cosmology: theory – dark matter

## 1 INTRODUCTION

In a  $\Lambda$ CDM universe, spiral galaxies consist of a disc component made of stars, cold gas and dust, a central bulge and a stellar halo, all embedded in a dark matter halo (White & Rees 1978). The disc component can be separated into two different parts: the thin disc, and the thick disc (Burstein 1979; Gilmore & Reid 1983). These two components are defined by examining the vertical scale height of stars when separated by age (e.g. Haywood et al. 2013; Bensby et al. 2014) or metallicity (e.g. Fuhrmann 2008; Bensby et al. 2014). The stars in the thin disc component are formed by gas accretion at the later stages of galaxy formation and they

have a wide range of ages (Yoachim & Dalcanton 2006). The stars in the thick disc, however, are older and their origin is still debated (e.g. Brook et al. 2004; Villalobos & Helmi 2008; Minchev et al. 2015).

The distribution of stars in galactic discs is also an ongoing research area. One of the favorite modes for the mass assembly of a galaxy is the “inside-out” scenario (Chiappini et al. 1997; Mo et al. 1998; Brook et al. 2012; Pilkington et al. 2012; Bird et al. 2013). In the inside-out growth proposal, the inner disc is thought to assemble first as a consequence of the high density of accreted gas residing in the center of the galaxy’s potential well. Thus, the fraction of young stars is expected to increase with galactocentric radius. Several galaxies have been found to be compatible with such a growth model (Pérez et al. 2013; Sánchez-Blázquez et al. 2014; Tacchella et al. 2015).

\* robert.mostoghiu@uam.es

† adicintio@iac.es

Recent observations regarding the ages of stars in the neighboring galaxy M33 indicate that this galaxy is compatible with an inside-out disc growth scenario, in which old stars are detected in the inner region of the galaxy, while young, disc stars tend to naturally be found in the outskirts of the disc (Williams et al. 2009; Barker et al. 2011). Specifically, these observations made use of the *Hubble Space Telescope Advance Camera for Surveys* (HST/ACS), to derive the cumulative star formation history (SFH) along M33's major axis and for different radii. The SFH was derived using the synthetic color-magnitude diagram (CMD) fitting method. CMDs were obtained by measuring resolved stellar photometry using the ACS module of the DOLPHOT software package (Dolphin 2000). Assuming an initial mass function and stellar evolution isochrones, a fitting is performed on the CMD to obtain the star formation rate at their respective ages and metallicities. Williams et al. (2009) and Barker et al. (2011) showed that within  $\approx 9$  kpc from M33's center, the mean age of stars decreases as one moves further out from the galactic center. They also showed that at radii greater than  $\approx 9$  kpc, however, this *age gradient* reverses, such that the mean age of stars increases as one approaches the outer region of M33. The age gradient thus reverses from decreasing mean stellar age with radius (within 9kpc) to increasing mean stellar age with radius (beyond 9kpc). Note that the age gradient reversal is accompanied by a surface brightness and stellar mass surface density break beyond 8 kpc (Ferguson et al. 2007; Barker et al. 2011), whose physics remains contentious (see Ruiz-Lara et al. 2017 for a recent review of the subject using simulations).

Similar age profiles have been seen in both simulations (e.g. Roškar et al. 2008a,b; Sánchez-Blázquez et al. 2009; Martínez-Serrano et al. 2009; Ruiz-Lara et al. 2016b) and observations of disc galaxies (e.g., Bakos et al. 2008; Yoachim et al. 2012; Zheng et al. 2015; Ruiz-Lara et al. 2016a), yet the origin of the reversal is not clear. Several explanations for the reversal have been proposed: stellar migration, in which the inner disc forms inside-out and the region beyond the upturn radius is populated with stars that migrated from the inner disc (Roškar et al. 2008a,b; Ruiz-Lara et al. 2016b); projection effects, that cause a contamination and overlap of stars from different galactic components (Barker et al. 2011); a decrease in the gas volume density in the disc, which induces a break in the star formation density which itself coincides with the radius where the gas disc begins to warp (Sánchez-Blázquez et al. 2009); or old stars coming from mergers that, due to their significant energy, remain in orbits at large, outer radii (Gill et al. 2005; Sales et al. 2007; Brook et al. 2012; Ruiz-Lara et al. 2016b).

In this paper we explore the age gradient of a simulated M33 analogue galaxy, formed in a constrained Local Group environment as part of the CLUES<sup>1</sup> project (Gottlöber et al. 2010; Carlesi et al. 2016). The initial conditions have been constrained by observational data such that the  $z=0$  cosmography is forced to reproduce the real local environment (Libeskind et al. 2015; Sorce et al. 2016). The simulated M33 analogue shares many properties with the observed M33 and was formed in a similar environment. This means that our analysis of the origin of the M33 analogue may provide in-

sights into the mechanisms driving the age gradient, in the real M33, in particular the reversal of the age gradient that is observed.

The paper is organized as follows. In Section 2 we present the simulated M33. In Section 2.1 we present the simulation's properties. In Section 2.2 we focus on the features of our candidate galaxy. The reversal of the age gradient in the SFH of M33 is presented in Section 3. In Section 3.1 we present the adopted methods to analyze the age reversal, in Section 3.2 we discuss the implications of our study, and in Section 3.3 we give observational predictions. Finally, in Section 4 we summarize our results.

## 2 A SIMULATED COUNTERPART OF M33

In this section we describe the properties of the M33 candidate found within one of the hydrodynamical numerical simulations performed as part of the *Constrained Local Universe Simulations* (CLUES) project (Gottlöber et al. 2010).

### 2.1 Constructing the numerical M33

In order to create constrained simulations of the Local Group (LG), the initial conditions are tuned using as observational constraints peculiar velocities obtained from the MARK III catalog (Willick et al. 1997), surface brightness fluctuations (Tonry et al. 2001), local volume galaxy catalogs (Karachentsev et al. 2004), and the position and virial properties of nearby X-ray selected clusters of galaxies (Reiprich & Böhringer 2002). Then, using the Hoffman-Ribak algorithm (Hoffman & Ribak 1991) and the observational constraints, the initial conditions are generated as constrained realizations of Gaussian random fields on a  $256^3$  mesh. Note that only large, linear scales are constrained: since they are non-linear, properties of the LG such as mass, relative positions and velocities, are unconstrainable. Therefore, low resolution initial conditions are run to  $z = 0$ , and those simulations which reproduce a structure resembling the LG are selected for high resolution resimulation. Numerical power is added following a zoom-in technique (Katz et al. 1994; Navarro & White 1994). The end result is a local group, selected in a frequentist manner, embedded in the proper constrained large scale structure. In the current work, the simulated LG includes a third galaxy which resembles M33 in terms of mass and placement, being at  $\approx 800$  kpc from the other two main halos.

The simulation was run using the standard  $\Lambda$ CDM *Wilkinson Microwave Anisotropy Probe 3* (WMAP3) cosmology (Spergel et al. 2007), with  $\Omega_M = 0.24$ ,  $\Omega_b = 0.042$ ,  $\Omega_\Lambda = 0.76$ ,  $\sigma_8 = 0.75$ ,  $h = 0.732$ , and an  $n = 0.95$  slope of the power spectrum. We used the parallel TreeSPH code GASOLINE (for further details see Wadsley et al. (2004a,b) and references therein) to simulate a cosmological box with side length  $L_{\text{box}} = 64h^{-1}$  Mpc, and effective particle resolution of  $m_{\text{DM}} = 2.1 \cdot 10^5 h^{-1} M_\odot$  and  $m_{\text{gas}} = 4.4 \cdot 10^4 h^{-1} M_\odot$ .

These hydrodynamical simulations have been presented and used to explore dwarf galaxies in the Local Volume (see Santos-Santos et al. 2016, 2017, where full details are found). In particular, the simulated galaxies were shown to match a range of scaling relations, including the relations between stellar and halos mass, stellar and HI gas mass, size

<sup>1</sup> [www.clues-project.org](http://www.clues-project.org)

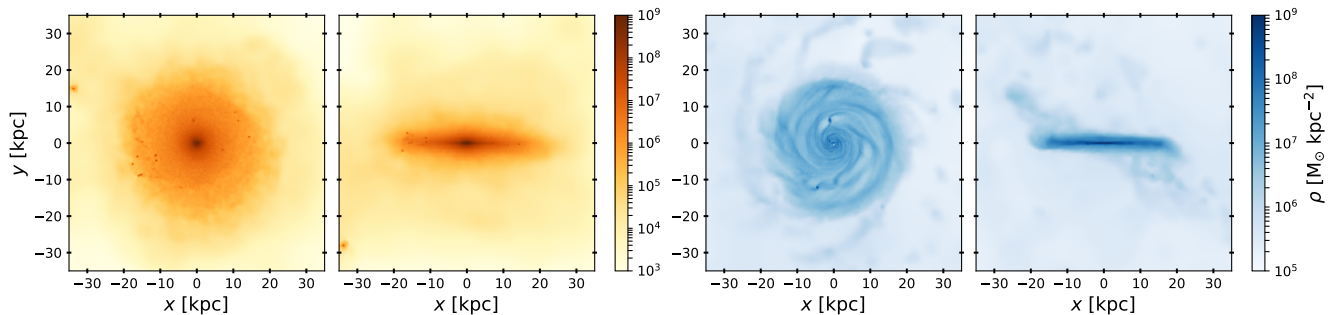


**Figure 1.** Stellar and gas mass densities of the simulated M33 galaxy at  $z=0$ . *Left:* stellar mass density, face-on and edge-on. *Right:* gas density, face-on and edge-on. Spiral features and a thin warped disc of gas are visible, in agreement with observational data (e.g. Corbelli & Schneider 1997; Kam et al. 2017).

and stellar mass, and the Tully-Fisher relation; meaning we can have a degree of confidence in our analysis. The simulations include a UV background, gas cooling, and star formation, with the stars feeding energy back into the interstellar medium (ISM) gas. Gas is eligible to form stars when it reaches temperatures below 15000 K in a dense environment, with minimum density threshold of  $10 \text{ amu/cm}^3$ . Blastwave supernova feedback is included à la Stinson et al. (2006), allowing an efficient regulation of star formation within galaxies. The stellar particles are formed with an initial mass of  $m_{\star} = 1.5 \cdot 10^4 h^{-1} M_{\odot}$ .

To identify halos in the simulation we used the MPI+OpenMP hybrid halo finder *AMIGA Halo Finder* (AHF)<sup>2</sup> (Gill et al. 2004; Knollmann & Knebe 2009), which locates local overdensities in an adaptively smoothed density field as potential halo centers and automatically identifies halos, subhalos, subsubhalos, etc. For every found halo, AHF calculates its virial radius  $r_{\text{vir}}$  as the radius  $r$  at which the density  $\rho(r) = M(< r)/(4\pi r^3/3)$  drops below  $\Delta_{\text{vir}}\rho_b$ , where  $\Delta_{\text{vir}}$  is a cosmological model and time dependent threshold parameter, and  $\rho_b$  is the cosmological background matter density. The threshold  $\Delta_{\text{vir}}$  is computed using the spherical top-hat collapse model. For the cosmology that we are using,  $\Delta_{\text{vir}} = 355$  at  $z = 0$  (Bryan & Norman 1998).

To trace halos through the snapshots we build merger trees with *MergerTree*, a tool that comes with AHF. *MergerTree* identifies counterpart objects in the same simulation at different redshifts. *MergerTree* follows each halo identified at redshift  $z = 0$  backwards in time, identifying as the main progenitor at some other redshift the halo that both shares the most particles with the present halo and is closest in mass. More details can be found in Srisawat et al. (2013).

Finally, for the analysis of the identified halos we used the Python-based package *PYNBODY*<sup>3</sup> (Pontzen et al. 2013).

## 2.2 Validating the numerical M33

In this sub-section we focus our attention on the M33 candidate found in the Local Group simulation, examining how

**Table 1.** Total virial mass and stellar mass of simulated and observed M33. Observational data from Corbelli et al. (2014); Kam et al. (2017), see text for more details.

M33	$M_{\text{vir}}(10^{11}M_{\odot})$	$M_{\star}(10^9M_{\odot})$	$M_{\text{HI}}(10^9M_{\odot})$
SIM	2.7	5.1	2.8
OBS	$4.3 \pm 1.0$	$4.8 \pm 0.6$	$1.9 \pm 0.4$

the properties of the candidate compare to the observed one. We start by showing, in Fig. 1, a visualization of the simulated galaxy at  $z=0$ , with the face-on and side-on views of the stellar and gas density of our M33 candidate. A warped disc component can be seen in the edge-on view, similarly to the warped disc reported in observations of M33 (e.g. Corbelli & Schneider 1997; Kam et al. 2017). Moreover, similar to the observed M33, our simulated counterpart shows well defined spiral features, clearly visible in the face-on gas density plot.

In order to compare more quantitatively with observational results, we present in Tab.1 the virial and stellar mass of the M33 candidate, and we compare these values with the observational M33 data reported in Corbelli et al. (2014) and Kam et al. (2017). For the simulation, the virial mass is computed as the total mass within the virial radius at  $z = 0$ , while the stellar mass is the sum of all the star particles found within the galaxy and its halo. We note that with a value of  $M_{\text{vir}} = 2.7 \cdot 10^{11} M_{\odot}$  and  $M_{\star} = 5.1 \cdot 10^9 M_{\odot}$ , our simulated M33 lies on the expected  $M_{\star}-M_{\text{halo}}$  relation, or abundance matching relation (e.g. Moster et al. 2010).

For the observed Triangulum galaxy, the virial mass and the stellar mass, together with the concentration of dark matter halo, are obtained by considering the composite probability of three events: the dynamical fit to the measured rotation curve of M33, the stellar mass determined via synthesis models, and the concentration-mass relation  $c(M)$  found in numerical simulations of structure formation for a  $\Lambda\text{CDM}$  cosmology (see Corbelli et al. 2014 for more details). Tab.1 indicates that our simulated M33 is very similar, in

<sup>2</sup> <http://popia.ft.uam.es/AHF>

<sup>3</sup> <https://github.com/pynbody/pynbody>

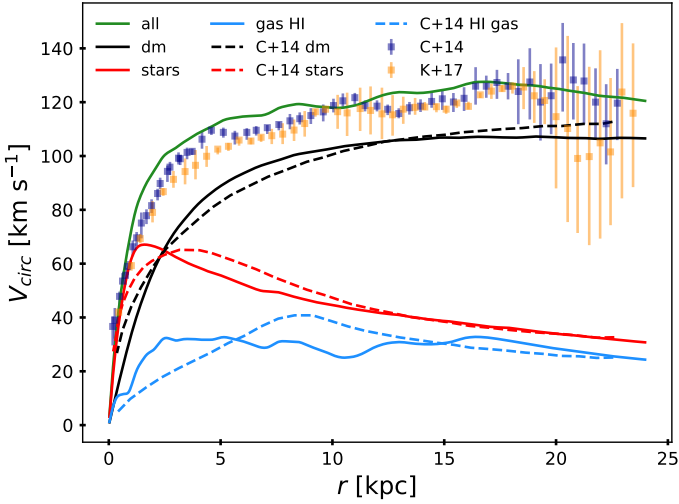


**Figure 2.** Circular velocity profiles of DM halo (black), stars (red) and HI gas (light blue) of the simulated M33 galaxy (solid lines) compared with observations from Corbelli et al. (2014) (dashed lines). The total velocity profile is shown in green for the simulated M33 and as blue and yellow points with error bars for the Corbelli et al. (2014) and Kam et al. (2017) data, respectively. The observed and simulated rotation curves agree within a few percents at all radii. See the online version for details.

both total and stellar mass, to the observed M33, justifying further comparisons.

In Fig.2 we study the mass component distribution of the galaxy, showing the circular velocity profile of dark matter (black lines), HI gas (light blue lines), and stars (red lines), alongside observations from Corbelli et al. (2014) and Kam et al. (2017). Observations are shown as dashed lines and simulations, as solid ones. The total velocity is shown as a green solid line for the simulated M33 and as points with error bars for the observed one. The simulated velocity profiles are computed by using the gravitational potential of the particles in the galactic midplane after placing the galaxy face-on using its total angular momentum. The HI gas component was obtained directly from the simulations, which solves the Saha equation to calculate the ionization state based on the pressure and temperature.

The total velocity curve matches the observed one quite well, reaching a maximum of  $V = 127.6$  km/s at a radius of  $r = 16.9$  kpc, like the real M33. However, some of the individual components have a rotation curve that rises faster in the innermost region of the galaxy, compared to the profiles derived from observational data in Corbelli et al. (2014). The HI gas component is closer to the observational data in the outer region of the galaxy ( $r \gtrsim 13$  kpc), while in the inner region it underestimates the peak velocity. Further, the slightly higher contribution from stars at the center of the simulated galaxy reflects the contribution of its larger-than-observed bulge (see below). Nevertheless, the overall agreement between the total simulated rotation curve and the observed one is quite good, with differences of a few per cent at most, depending on the radii.

Our last comparison to observations will now go into even more details by mimicking observations as closely as

possible. We therefore set the simulated M33 in a configuration which resembles the observed one. Starting from an initial face-on view, where the disc lies on the  $xy$  plane, we inclined the M33 candidate 60 degrees around the  $x$ -axis to reach the reported inclination of M33 to the line of sight from the Earth,  $i \approx 50^\circ - 60^\circ$  (e.g. Patterson 1940; Verley et al. 2009). Furthermore, since observational data has been measured along the major axis of the galaxy to avoid stellar contamination from different galactic components, we select the major axis of the inclined simulated M33 in a similar fashion by applying a position cutoff in the axis perpendicular to the inclination axis, i.e. we select star particles with  $|y| \leq 5$  kpc. Note that, since our galaxy is not circularly symmetric, there is a degeneracy in the initial face-on view of the galaxy; different initial face-on views (as generated by rotations about our  $z$ -axis) produce different profiles of projected quantities after inclining the galaxy. For our analysis we selected a face-on view which best reproduces the observed surface brightness profile<sup>4</sup>, to be discussed now.

Once the simulated M33 is in its inclined configuration, we performed a bulge/disc decomposition in order to compute the galaxy’s disc scale length (for a detailed description of the analysis, see Appx. A). We fit the  $i$ -band surface brightness profile of the galaxy with a 3-component model, i.e. a combined inner and outer exponential discs plus a Sersic bulge, to account for breaks in the profile. We obtain an inner disc scale-length of  $h_d = 3.3 \pm 0.1$  kpc. The observed M33 has a somewhat shorter scale length for the disc,  $h_d^{M33} = 1.8$  kpc (Verley et al. 2007; Ferguson et al. 2007; Verley et al. 2009; Corbelli et al. 2014). To account for this difference and in order to compare our simulated profiles with the observational data, respectively, we normalize the  $x$ -axis to the respective inner exponential disc scale length and the  $y$ -axis to the respective value at that position. In Fig. 3 we show the (normalized) surface brightness profile. Along the simulated profile, we present the observed  $i$ -band surface brightness profile from Ferguson et al. (2007). We find the best match to observational data within the region  $0.9 < r/h_d < 4.5$  (or in physical units  $3 < r < 15$  kpc) – as indicated by the two vertical dashed lines. In the inner region of our numerical M33 ( $r \lesssim 3$  kpc, left dashed line), we can identify an excess of light from the bulge component. From  $r \gtrsim 15$  kpc onwards (as indicated by the right dashed line), the M33 candidate follows closely the observed light distribution. Additionally, the simulated profile features a down-bending disc break at  $r \sim 5.3h_d = 17.6$  kpc, which correlates with the radius at which the age reversal is found (see Sec. 3). The disc break in the observational profile is found at a similar (although slightly smaller) position, at  $r = 4.5h_d^{M33} = 8.1$  kpc. Following Martín-Navarro et al. (2012, 2014), at  $r \sim 7.6h_d = 25$  kpc we can also identify an up-bending in the surface brightness profile associated with the stellar halo component of the simulated galaxy, coexisting with a truncation, i.e. a sharp decline in the radial light profile, that allows the stellar halo component to outshine the disc’s light distribution. We note that we obtain similar results in the stellar surface mass

<sup>4</sup> We studied 36 initial  $z$ -axis rotations of the initial face-on view, spanning 360 degrees, and found that  $\sim 64$  per cent of the initial configurations present a strong break in the profile, while the rest show weak-to-null breaks after the 60 degree rotation.

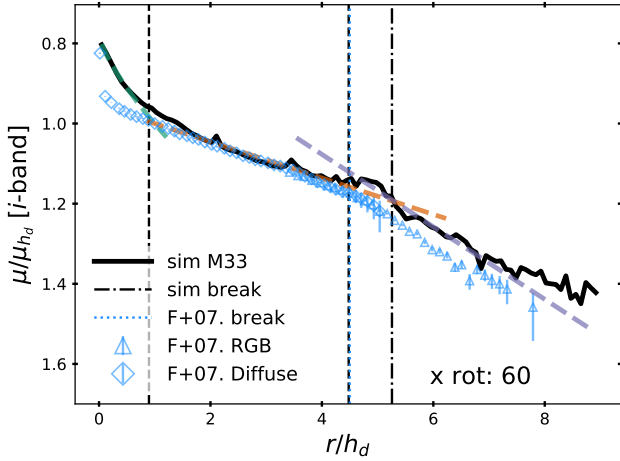


**Figure 3.** Surface brightness of the simulated M33 for the inclined configuration, normalized by the value at the inner disc’s scale radius  $h_d$ . The best-fit values of the 3–component fit (colored dashed lines) are presented in Tab. A1. The vertical black dashed lines show the  $r = 3$  kpc and  $r = 15$  kpc regions. Observational values from Ferguson et al. (2007) are represented as blue markers, with its corresponding break at  $r = 4.5h_d^{M33} = 8.1$  kpc (blue dotted line, on top of the  $r = 4.5h_d = 15$  kpc dashed line). Similar to what is observed in the real M33, a break can be seen in the simulated galaxy at a similar position,  $r \sim 5.3h_d = 17.6$  kpc (black dash-dotted line), as well as a truncation at  $r \sim 7.6h_d = 25$  kpc.

density profile of the simulated galaxy (not shown here): the 3–component fit leads to a comparable inner disc scale length, and we identify a break and a truncation at the same radii. The fact that we observe a break in the both profiles suggests that the reversal in the age gradient is affected by the combined effect of both the radial distribution of the star particles and their ages and metallicities.

We have just demonstrated that our numerical M33 is in fact an adequate replica of the observed M33: it is situated in the right environment, has about the correct size and mass, features comparable kinematics, and even agrees fairly well when observed from the right angle. And as we will see in the next Section, it also features the observed reversal of the age gradient. This motivated us to seek its origin using the constrained simulation of the Local Group and its constituent M33. However, we like to close with the cautionary note that even though our numerical M33 appears to be a reasonable counterpart of the observed one, we need to remind the reader that it is by far a facsimile. As mentioned before, the very nature of following non-linear cosmic structure by means of numerical simulation only allows constraining scales beyond the size of the Local Group; random fluctuations will always enter scales smaller than that. For an elaborate discussion of such effects and restrictions we like to refer to the work of Carlesi et al. (2016) where the ‘Local Group Factory’, i.e. a framework for simulating the ‘near field’, has been presented.

### 3 THE REVERSED STELLAR AGE GRADIENT IN M33

In the previous section we examined some specific properties of our M33 candidate, and we showed that, despite some unavoidable differences we are able to reproduce fairly well the morphology, luminosity, mass and velocity curve of the observed M33 galaxy. But one of the strongest arguments for studying the numerical M33 in our simulated LG is that we found a similar reversal of the age gradient in the cumulative normalized SFH of the simulated M33, as observations report (e.g. Williams et al. 2009; Barker et al. 2011). In the next sections we present our analysis of this phenomenon.

#### 3.1 Presentation of the Radial Stellar Age Gradient

In Fig. 4 we show the combined observational results of the cumulative normalized SFH of M33, as reported in Williams et al. (2009) and Barker et al. (2011), referred to as W09+B11 from now on. The observations were made along the major axis of M33 using the HST/ACS in the Wide Field Channel, with field of view of  $202'' \times 202''$ , at radii of  $r = 0.9, 2.5, 4.3, 6.1$  kpc in Williams et al. (2009), and later extended to  $r = 9.1, 11.6$  kpc by Barker et al. (2011). As we move further out from the galactic center the intermediate-to-old star population fraction decreases while young stars start contributing more and more to the overall budget in the outer disc, compatible with an inside-out growth. Within 0.9 kpc from the galactic center, more than 70 per cent of stars are old, having formed in the first 4 Gyrs of the galaxy assembly, while less than 10 per cent of the stars found at a radius of 6.1 kpc are old. At 9.1 kpc, more than 80 per cent of the stars are young, specifically younger than 4 Gyrs.

However, as already noted in Barker et al. (2011), once the radius  $r = 11.6$  kpc is reached (in magenta), the curve shifts to lower  $t$  with respect to  $r = 9.1$  kpc (in yellow), i.e. the fraction of old stars increases again. Indeed, at 11.6 kpc stars are found that are older than the oldest population at  $r = 9.1$  kpc, even after considering the  $1\sigma$  error (dashed lines). Such an age gradient reversal, with increasing mean stellar age with radius, thus happens for radii beyond 9 kpc.

In order to compare our galaxy to observations we analyze the star particles in our halo in a similar fashion to the measurements done in W09+B11. After positioning the simulated galaxy face-on, we choose a series of concentric annuli of thickness  $\delta_{\text{ann}} = 0.8$  kpc, similar to the field of view of the camera used in W09+B11, centered at the same radii of Fig. 4,  $r_{\text{obs}}$ , for which observations exist. The annuli’s radii will then be  $r_{\text{ann}} = r_{\text{obs}} \pm \delta_{\text{ann}}/2$ , where  $r_{\text{obs}} = 0.9, 2.5, 4.3, 6.1, 9.1, 11.6$  kpc. We further extend the sampling region up to  $r_{\text{ann}} = 30$  kpc, in order to cover even the outer part of the disc, for which observations of the M33’s SFH currently do not exist. We choose annular regions in order to avoid a definition of a major axis and to get a statistically meaningful result. In order to check that our results are insensitive to – and not driven by – the inclination of the galaxy, we repeat the same analysis for our (best) inclined configuration described in Sec. 2.2.

In Fig. 5 we show the annular regions used to compute

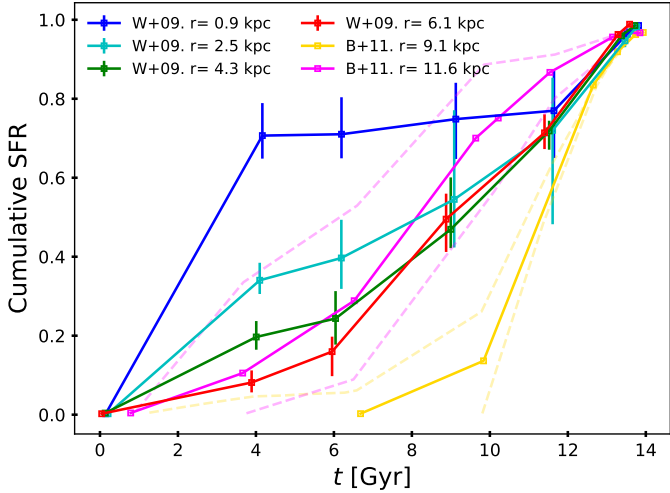


**Figure 4.** Cumulative normalized SFH of the M33 galaxy measured along its major axis. Data retrieved from [Barker et al. \(2011\)](#) with results from [Williams et al. \(2009\)](#), presented in a revised form for direct comparison with our simulation. The dashed lines represent the  $1\sigma$  contours for the last two radial bins. As we move further out from the galactic center the young stellar population increases, compatibly with an inside-out growth of the disc. Between  $r = 9.1$  kpc and  $r = 11.6$  kpc, however, a significant shift is found to older age (smaller  $t$ ), signifying a reversal in the galactic radial age gradient, that is, the stellar radial age gradient of the galaxy reverses. See the online version for details.

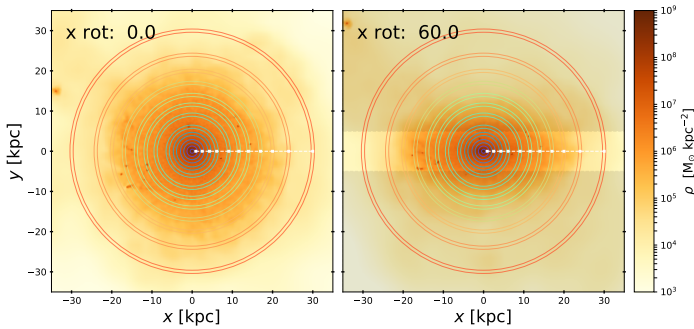


**Figure 5.** Concentric annuli spanning a region between 0.9 to 30 kpc from the galactic centre, chosen to select the star particles used to compute the SFH of our M33 candidate. The annuli are shown superimposed on the stellar mass density plot. The SFH at different radii will be computed for two configurations of the galaxy: face on, *left panel*, and after a rotation of  $60^\circ$ , *right panel*. In this last case, we only considered the star particles within the annuli around the major axis of the galaxy, identified as a bright area in the right panel, i.e. the region where the bulk stellar mass density resides,  $|y| < 5$  kpc.

the SFHs<sup>5</sup>, superimposed on the stellar mass density of our simulated galaxy, for the face-on view (left panel), and for

<sup>5</sup> Considering that star particles migrate from their birth position, technically we calculate the Stellar Formation Time Distribution of the M33 look-alike at  $z = 0$ . For clarity, we will maintain the SFH nomenclature throughout the paper.

the inclined view (right panel). For this latter setup, instead of taking the star particles in the whole annular regions as done for the face-on analysis, we select the ones in the annular regions within the major axis ( $|y| < 5$  kpc) for this configuration. The area of the annuli that we consider in this case is indicated as a bright region in the right panel of Fig. 5. Once the annuli are defined, the star particles inside them are selected and used to calculate the SFH at each radius<sup>6</sup>.

In Fig. 6 we show the results of the SFH analysis of the simulated M33, presented analogously to the observational data in Fig. 4, as cumulative SFHs at different radii, for the galaxy viewed face-on (left panel) and for the  $60^\circ$  inclined view (right panel). Increasing radii are shown in different colors, from violet (0.9 kpc) to red (30 kpc). Moving from the inner radii to the outer ones, the mean stellar age decreases, compatible with an inside-out growth of the disc.

However, at radii larger than  $r = 17$  kpc a reversal of the age gradient is observed in both the face-on and the inclined view, just as found in observations, with the percentage of old stars that contribute to the SFH rising again. The reversal region reported in W09+B11 ( $r > 9.1$  kpc) is smaller than the one found in our simulation: this should not be surprising given the different scale-lengths of the observed and simulated M33. In terms of relative disc scale lengths, the age reversal appears at a radius of about 5.1 times the disc scale length in the observed M33, and 5.2 times in the M33 look-alike. As mentioned in the previous section, we note that a break in the surface brightness and stellar surface density profiles of our M33 candidate appears at a radius  $r = 17.6$  kpc, coinciding with the radial region at which the age turnaround is found, which suggest that a correlation between the two effects could exist, similar to what has been discussed in W09+B11.

Comparing the inferred region of the reversal radius of the face-on and inclined views, we expect that projection effects in the inclined view would move the reversal radius closer to the galactic center after rotating the galaxy. The reversal region is instead found between  $r = 17$  and  $r = 20$  kpc (dashed lines) for both configurations. However, analyzing the surface brightness and stellar surface density profiles of the face-on view, we indeed find that the break moved to  $r \sim 19$  kpc (still within  $17 < r < 20$  kpc). Thus, inspecting the cumulative SFH only provides a rough estimation of the turnaround radius' location, that is, it constrains the boundary of the region in which the turnaround radius is found. The age reversal detected in observations could be similarly affected by the inclination of the galaxy itself and subsequent projection effects. Indeed, with a  $60^\circ$  inclination with respect to the line-of-sight, the old stars in the outer region will overlap with the young stars in the disc, causing a higher contribution of old stars at smaller radii. This effect can be seen in the median formation time of the  $r = 14.0$

<sup>6</sup> Each annular region is further subdivided in smaller regions, each subtending an arch of 0.8 kpc across as we spam the  $360^\circ$  angle around each annuli, to mimick the size of the HST/ACS field of view. We perform the SFH analysis for such individual regions, as well as for the total amount of stellar particles within each annuli, in order to confirm that our results are not affected by a specific position within each annuli.

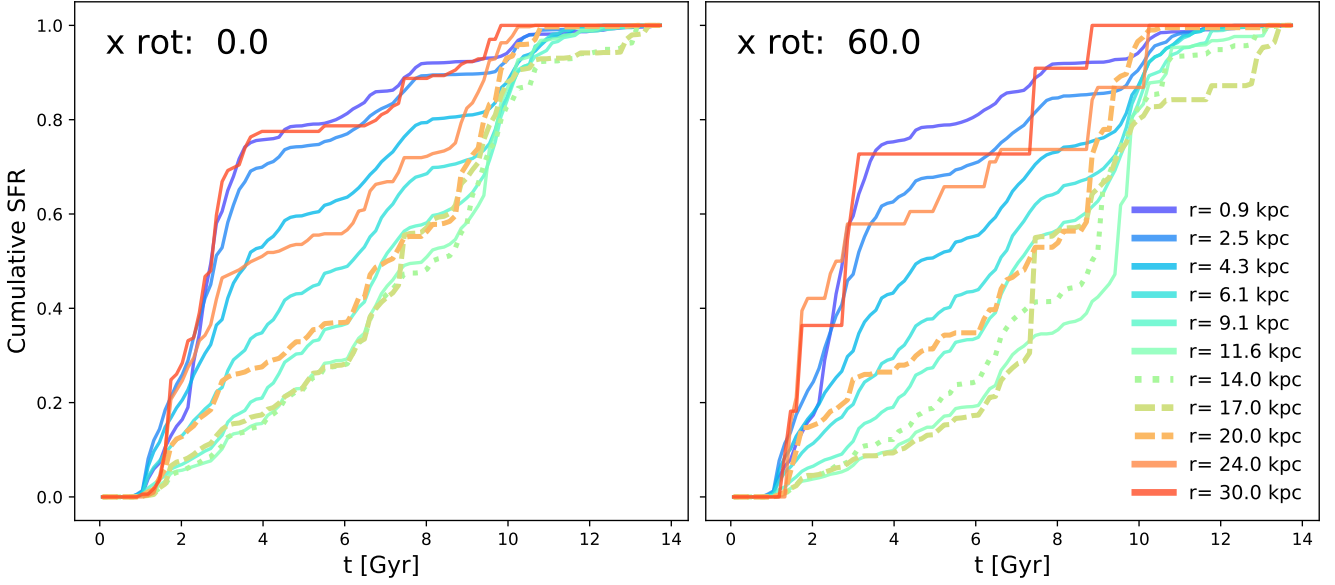


**Figure 6.** The cumulative normalized SFH of the simulated M33 galaxy, for several increasing radii out to a maximum radius of 30 kpc. *Left:* SFH for the galaxy positioned face-on. *Right:* SFH after a  $60^\circ$  rotation around the  $x$ -axis of the galaxy. In both cases, moving inside-out the median stellar age decreases, compatibly with an inside-out growth of the disc. However, a reversal in the age gradient can be seen at large radii, where an increasingly higher fraction of old stars contributes to the SFH. In both the face-on and the inclined case, the radius at which the age reversal appears is between  $r = 17$  kpc and  $r = 20$  kpc (dashed lines). Projection effects may lead to a misidentification of the reversal radius, as seen from the median stellar age at  $r = 14$  kpc (dotted line).

kpc region (dotted line), which shifted to a slightly older population after the inclination.

We conclude that a reversal in stellar age gradient appears for our M33 candidate with respect to the line-of-sight, and that the value of the reversal radius is sensitive to the particular inclination chosen, being smaller for larger inclinations. While this change is not observed directly in the SFH of the face-on and inclined views of the galaxy, considering the correlation between the reversal radius and the break radius we are able to trace the projection effects through the break radius. Therefore, the deprojected reversal radius of the observed M33 may be at a different position than the one currently reported.

### 3.2 Explanation of the Stellar Age Gradient

As already touched upon before, there are several hypothesis that could explain the reversal of the stellar age gradient, such as mergers and stellar radial migration. To investigate which process determines the age turnaround in our simulation, we select the star particles that are within the M33 host at  $z = 0$  and trace them back in time to their birth redshift  $z_{\text{birth}}$  and position  $r(z_{\text{birth}})$ , respectively.

Then, by looking at their  $r(z_{\text{birth}})/R_{\text{vir}}^{M33}(z_{\text{birth}})$  distribution, we were able to identify a main population of stars in the inner region of the galaxy, well separated from an outer stellar population found beyond 20 per cent of M33’s virial radius. Thus, we define *in-situ* star particles as those that formed within 20 per cent of the virial radius of the main progenitor of M33 at the formation redshift, that is, whose birth radius satisfies the condition  $r(z_{\text{birth}}) < 0.2 \times R_{\text{vir}}^{M33}(z_{\text{birth}})$ . If, instead, the star particle has a birth radius larger than the

above value it is defined as *accreted*, since it is brought into the main M33 galaxy via mergers and halos accretion. We performed some tests to check our selection criterion. We used a different classification of ‘in-situ’ versus ‘accreted’ stars by checking whether a star particle was born in the progenitor of M33, inside a subhalo, or outside the progenitor’s virial radius. We also cleaned the disc from highly eccentric orbits that are not compatible with stars formed in the disc by making an eccentricity and vertical ( $z$ -component) velocity cut at  $z = 0$  of  $e < 0.6$  and  $|v_z| < 150$  km/s, respectively. We confirm that our tests had no influence on the results presented here and that the virial radius condition is sufficient to ensure that the star particles are formed within the disc of the progenitor of M33.

In Fig. 7, we show the projected (2D) median formation time for all (red solid line), in-situ (green dash-dotted line) and accreted (blue dashed line) star particles, as a function of radius (normalized by the disc scale length to correct for the size of the galaxies), for the inclined view of the M33 candidate. Along the simulated results we show the inferred median formation time profile from W09+B11 (color-coded markers), i.e. the formation time at which half of the cumulative SFR is reached at each radius. As we can see in the figure, the break radius of our simulation (dash-dotted black line) lies within the region of the turnaround radius inferred from the cumulative SFH (gray shaded region). Moreover, the maximum formation time (minimum age) of each profile is located at a similar relative projected radial positions, at  $r_{\text{max,tf}} \sim 4.5h_d \sim 15$  kpc for the simulated profile, and at  $r_{\text{max,tf}}^{M33} \sim 5h_d^{M33} \sim 9.1$  kpc for the observed one; and at a similar projected radius to their respective break radii, at  $r_{\text{break}} \sim 5.3h_d \sim 17.6$  kpc for the M33

candidate, and at  $r_{\text{break}}^{M33} \sim 4.5h_d^{M33} \sim 8.1$  kpc for the real M33. Once we scale the radial dependence of the profile to the corresponding disc scale length, the results are in good agreement with the observational trends. However, this has been done for a particular inclined initial configuration (i.e. our best configuration as introduced in Sec. 2.2). Although we obtain similar trends to the observational data, we are aware of the statistical limitation of the analysis. While the age turnaround is evident when considering the full sample of stars, with a median formation time decreasing from a maximum of  $t_f \sim 8$  Gyrs at  $r_{xy} \sim 4.5h_d$  ( $r_{xy} = 15$  kpc) to a minimum of  $t_f \sim 3$  Gyrs at  $r_{xy} \sim 9.1h_d$  ( $r_{xy} = 30$  kpc), such a turnaround does not show up when only in-situ star particles are considered. Hence, the main driver of the reversal is not due to in-situ star particles, but rather to accreted ones. As we move further out from the galactic center, the in-situ stars become progressively younger until reaching a radius of  $r_{xy} \sim 4h_d$  ( $r_{xy} \sim 13$  kpc), after which their age distribution flattens, with a median age of 4.7 Gyrs ( $t_f \sim 9$  Gyrs) for radii larger than 13 kpc. Note that, in an inside-out formation scenario we expect a monotonic increase of the formation time of the in-situ star particles with increasing radii, thus, the flattening of the profile clearly demonstrates that stellar migration also plays a role in the stellar age gradient of our simulated M33 (we will return to this point later). The same trends can be seen in the (3D) median formation time profile of the galaxy, as presented in Fig. 8: a turnaround in the whole star population at  $r > 15$  kpc, a formation time flattening of the in-situ population, and an old flat distribution of star particles up to  $r < 30$  kpc; with the only difference being the actual median formation time values of each component. In light of these results, in the following section we opted for a full 3D analysis of the origin of the turnaround.

Star particles that get into the galaxy via mergers are the main drivers of the observed age turnaround. The relative fraction of in-situ and accreted star particles within radial bins are shown in Fig. 9: the in-situ star fraction within 3 – 15 kpc is  $\sim 80$  per cent, while it decreases sharply as we move towards the outskirts of the galaxy, with a minimum of 20 per cent star particles found at  $r = 30$  kpc being in-situ. The fraction of accreted stars, correspondingly, increases with radius: in the turn-around region, the accreted star fraction move from less than 20 to almost 80 per cent. We verified that the accreted stars that end up in the age reversal region (at  $r > 15$  kpc) are brought in through minor mergers. Instead, the peak of accreted stars seen in the inner radii, at  $r = 3-4$  kpc, is attributable to the last major merger that occurred in the early phases of the life of the galaxy, before  $z = 2$ .

To investigate the role of accreted stellar particles as a function of their age, we first aim at classifying the stars by their actual formation time. To this extent we present in Fig. 10 the total, integrated SFH for the simulated M33 analogue at  $z = 0$ . We can observe several star forming bursts along its evolution. These bursts allow us to divide the stars into the following formation time bins: an old population of stars with  $0 < t_f \leq 4$  Gyr, a old-to-intermediate stellar population corresponding to a small burst with  $4 < t_f \leq 6$  Gyr, an intermediate-to-young stellar population with  $6 < t_f \leq 8$  Gyr, and the rest of the stellar population with  $t_f > 8$  Gyr

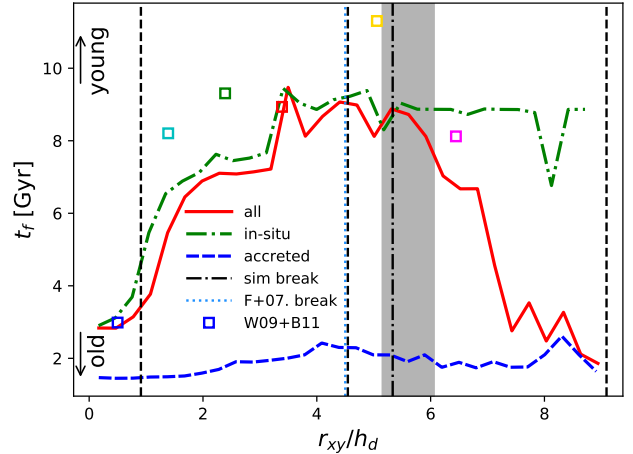


**Figure 7.** Projected (2D) median formation time of star particles in the inclined view, for increasing radial bins normalized by the disc scale length. The formation time profile of all star particles within M33 at  $z = 0$  is shown as a red line, while in-situ and accreted stars are shown as green dash-dotted and blue dashed lines, respectively. Vertical dashed lines indicate the pre-turnaround (3-15 kpc) and the turnaround region (15-30 kpc) of the galaxy. The inferred median formation time for different radii from W09+B11 is shown as the color-coded markers. The blue vertical dotted line shows the surface brightness break radius from Ferguson et al. (2007), whereas the black dash-dotted vertical line shows the break radius in the M33 look-alike. The inferred age turnaround radius from the SFH of the M33 candidate in Fig. 6 is represented by the gray shaded region. Note that the age turnaround disappears when only in-situ star particles are considered.

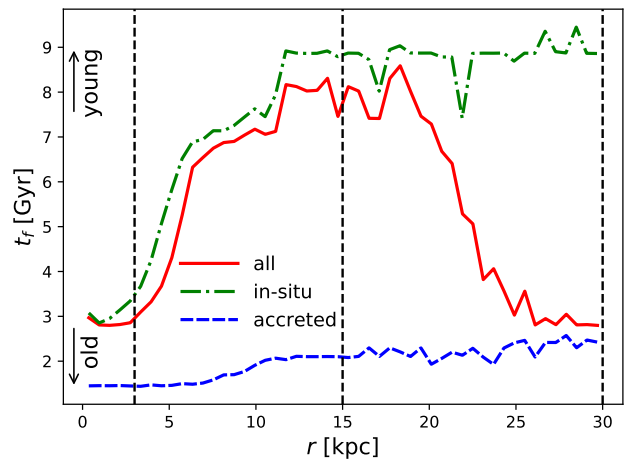


**Figure 8.** 3D median formation time of star particles for increasing radial bins. We can see similar trends as the ones identified in the projected (2D) median formation time profile in Fig. 7: a turnaround in the whole star population at  $r > 15$  kpc, a formation time flattening of the in-situ population, and an old flat distribution of star particles up to  $r < 30$  kpc. The fraction of in-situ stars within these regions is shown in Fig. 9.



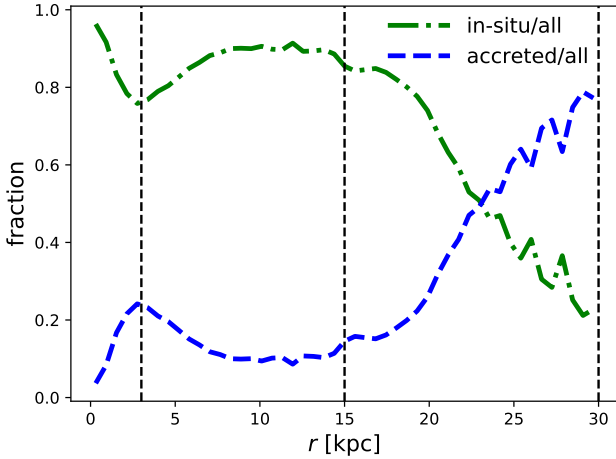


**Figure 9.** Fraction of in-situ and accreted stellar particles within radial bins, found in the simulated M33 at  $z=0$ . The in-situ stars made up  $\sim 85$  per cent of the total stellar mass within  $r = 15$  kpc, while at larger radii their fraction decreases dramatically to about  $\sim 20$  per cent for  $r = 30$  kpc. Correspondingly, the fraction of stars accreted via mergers increases with radius, causing the age-reversal observed at large radii. The peak of accreted stars seen in the inner radii, at  $r = 3 - 4$  kpc, is attributable to the last major merger that occurred in the early phases of the life of the galaxy, before  $z = 2$ .

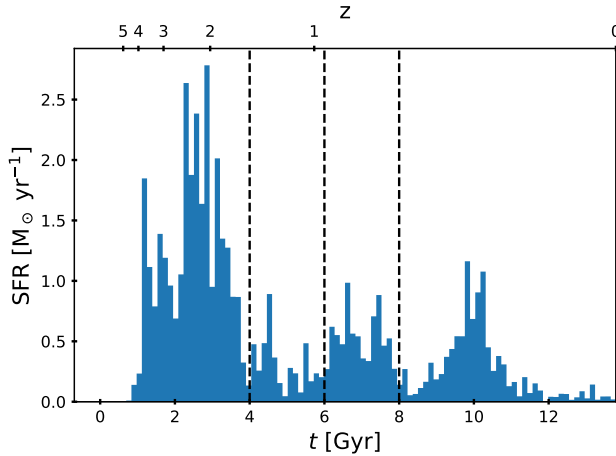


**Figure 10.** Integrated SFH of the simulated M33. We indicate the stellar age bins that will be later used for further analysis, selected following the main bursts of star formation.

corresponding to the last major stellar burst. We then show, in Fig. 11, the percentage of in-situ star particles in the pre-turnaround region,  $3 < r \leq 15$  kpc (top row), and in the turnaround area  $15 < r \leq 30$  kpc (bottom row)<sup>7</sup>. From left to right, we indicate the full percentage of in-situ stars, and the relative percentages of in-situ stars once binning by for-

<sup>7</sup> Since we are interested in disc-stars, we avoid the central bulge region of our simulated galaxy when computing percentages, and select star particles with  $r > 3$  kpc.

mation time  $t_f$ . In-situ star particles account for  $\sim 85$  per cent of the total stellar mass in the inner region of M33, and only for  $\sim 74$  per cent of the total star mass in the outer region. Therefore, the total accreted star particle fraction increases from  $\sim 15$  to  $\sim 26$  per cent when moving towards the outskirts of the galaxy. As expected for an inside-out growth scenario, almost all the stars with a formation time  $t_f > 4$  Gyrs are born in-situ, at any radial region. While, strikingly, only about  $\sim 7$  per cent of the old stars ( $t_f \leq 4$  Gyrs) found in the outskirts of M33 ( $15$  to  $30$  kpc), where the age turnaround is observed, are in-situ star particles. In the radial region corresponding to the observed age reversal,  $\sim 93$  per cent of the stars with old formation time are accreted via mergers, being the cause for the turnaround in the formation time profile.

Next, to verify whether stellar migration also plays a role in the age reversal, we quantify the amount of radial migration that has taken place in the disc. To this extent, we need to estimate the change in angular momentum, which is equivalent to the change in guiding radius ( $r_g$ ) since a star particle's formation time. We approximate  $r_g$  for each star particle as described in Minchev et al. (2014) by calculating the birth and end guiding radii as:

$$r_g = \frac{L}{v_{\text{circ}}(r)} = \frac{r \cdot v_\phi}{v_{\text{circ}}(r)}$$

where  $L$  and  $v_\phi$  are the angular momentum and rotational velocity of the star particle, respectively, and  $v_{\text{circ}}$  is the rotation curve. The guiding radius takes into account stars with high eccentricity orbits by comparing the star's tangential circular velocity,  $v_\phi$ , with the circular velocity of the galaxy at the star's radius,  $v_{\text{circ}}(r)$ . This allows us to know the change in the angular momentum of the star particles, which is equivalent to the change in the guiding radius at  $z = 0$  ( $r_{g,\text{end}}$ ), and the guiding radius at the birth redshift of the star particle ( $r_{g,\text{birth}}$ ). By using the guiding radius we avoid mistaking stars with high eccentricity orbits as instances of radial migration.

We now present in Fig. 12 the guiding radius at  $z = 0$  ( $r_{g,\text{end}}$ ) vs. the guiding radius at the birth redshift ( $r_{g,\text{birth}}$ ) for the star particles that were born in M33's main progenitor, i.e. in-situ ones, selected from two regions in the formation time profile,  $3 < r \leq 15$  kpc (top row) and  $15 < r \leq 30$  kpc (bottom row), further separating the stars using aforementioned formation time bins (from left to right, we move from old to young stars). Black dashed lines indicate the locus of stars that have not changed their position, i.e. whose guiding birth radius  $r_{g,\text{birth}}$  is the same as their end one  $r_{g,\text{end}}$ . In the inner region, most of the old,  $t_f \leq 4$  Gyr, population moved to slightly greater radii ( $\sim 70$  per cent of stars moved from  $r_{g,\text{birth}} \sim 0.5 - 1.5$  kpc to  $r_{g,\text{end}} \sim 2 - 4$  kpc), whereas almost all the younger stars ( $t_f > 4$  Gyr) remained close to where they were born, i.e. close to the black dashed line. Thus, radial migration is observed to some extent for the old population of in-situ stars in the inner region of the galaxy: their final guiding radius, however, it is still smaller than the radius at which the age turnaround is found.<sup>8</sup> In

<sup>8</sup> Note that we initially selected the star particles by their radius

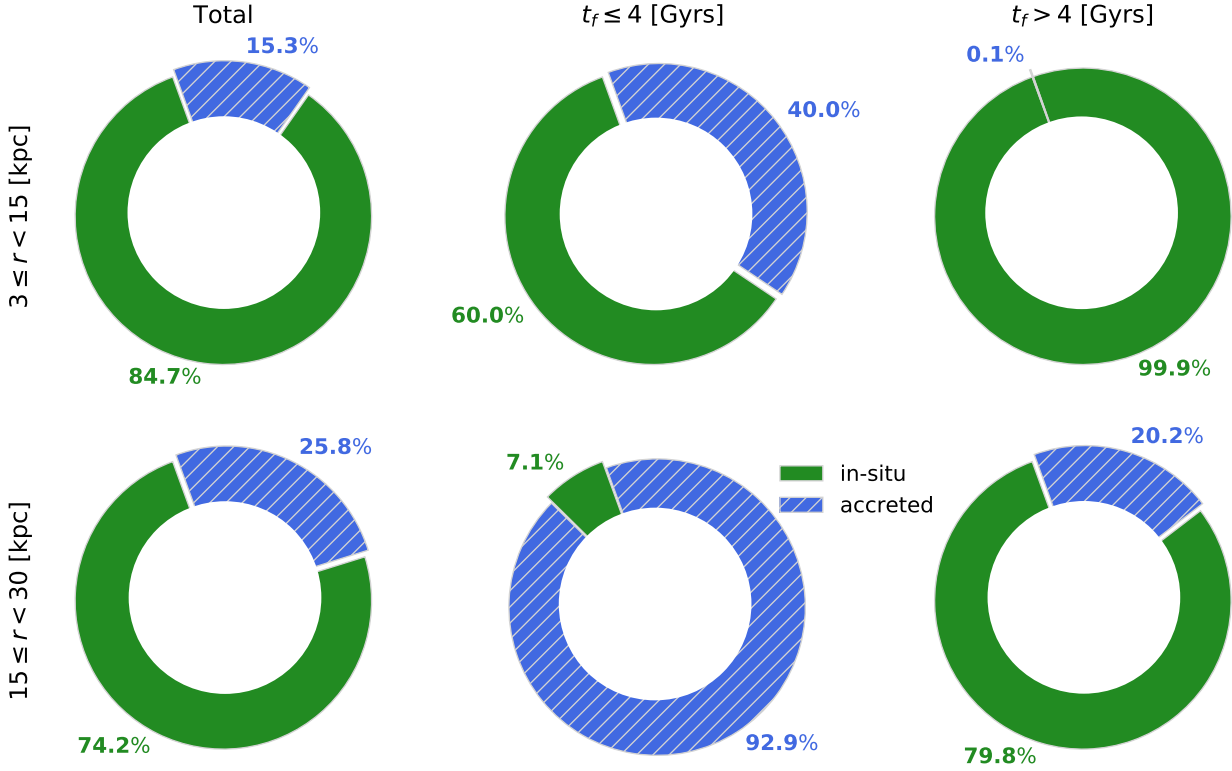


**Figure 11.** In-situ star particles percentages in the pre-turnaround region ( $3 < r \leq 15$  kpc, top row) and in the turnaround region ( $15 < r \leq 30$  kpc, bottom row). Only about  $\sim 7$  per cent of the old stars ( $t_f \leq 4$  Gyrs) found in the outskirts of M33 ( $15$  to  $30$  kpc), where the age-turn around is observed, are in-situ star particles.

the outer region, however, we see a considerable radial migration for the old population ( $t_f < 4$  Gyr), most of which migrate from  $r_{g,\text{birth}} \sim 0$  kpc to  $r_{g,\text{end}} \sim 12 - 17$  kpc, and few of them reaching as far out as  $r_{g,\text{end}} \sim 20$  kpc. The rest of the stellar populations present less and less radial migration the younger they are. Thus, the old in-situ stars, which made up only the 7 per cent of the old stars found in the outer region of M33, have undergone thorough radial migration, i.e. they are stars that were born close to the galaxy’s disc plane center and have migrated outwards. However, given their small number compared to the fraction of old accreted stars, migration of in-situ stars alone is not sufficient to explain the age turnaround found in Fig. 8: without accretion we could not observe this age reversal. Hence, we conclude that the main driver behind the reversal of the age gradient is stellar accretion and, to a lesser extent, stellar migration.

### 3.3 Observational predictions

In order to verify that the age turnaround is mainly driven by stellar accretion, one would need to be able to differen-

$3 < r \leq 15$  kpc, and by using the guiding radius  $r_g$  we find stars with  $r_{g,\text{end}} < 3$  kpc, outside the originally selected region at  $z = 0$ . This indicates that in this region there are some star particles that are on highly eccentric orbits. Although we find them at a particular radius at  $z = 0$ , their guiding radius reveals they have different average radii.

tiate – observationally – accreted from in-situ stars. Since both groups of stars share the same location in the galaxy at  $z = 0$ , we must rely on their kinematics for this aim. In this section, we investigate the kinematic properties of the two populations of star particles found in the outer region of our simulated Triangulum galaxy.

Using the same (best) inclined configuration of our numerical M33, we study the line of sight velocity  $V_{\text{los}}$  of the star particles in the disc. We selected the projected star particles within a square region of 4 kpc in side, alongside the major axis of M33, centered on the age turnaround region,  $16 \leq x \leq 20$  kpc and  $|y| \leq 2$  kpc. To improve the sample of stars, and to avoid any preferential direction on the major axis, we performed the selection for both the right-hand side ( $x > 0$ ) and the left-hand side ( $x < 0$ ) of the galaxy, and combined the selected stars taking into account the sign change due to the rotation of the star particles in the disc. We then plotted a histogram of the star particles’ line of sight velocity  $V_{\text{los}}$  (in projection, identified with the  $z$  axis-component of the star particle’s velocity), in Fig. 13. The total, in-situ and accreted stars, are shown as red, green and blue histograms, respectively, along the number of stars in each category. The vertical dashed line at  $V_{\text{los}} \sim 109$  km/s is the galaxy’s circular velocity corrected for inclination. The difference between the accreted star particles and the in-situ ones is clear: while the latter are co-rotating with the disc, with a peak rotation of  $V_{\text{los}} \sim 94$  km/s and a relatively small velocity dispersion,  $\sigma \sim 19$  km/s, the accreted stars have randomly distributed

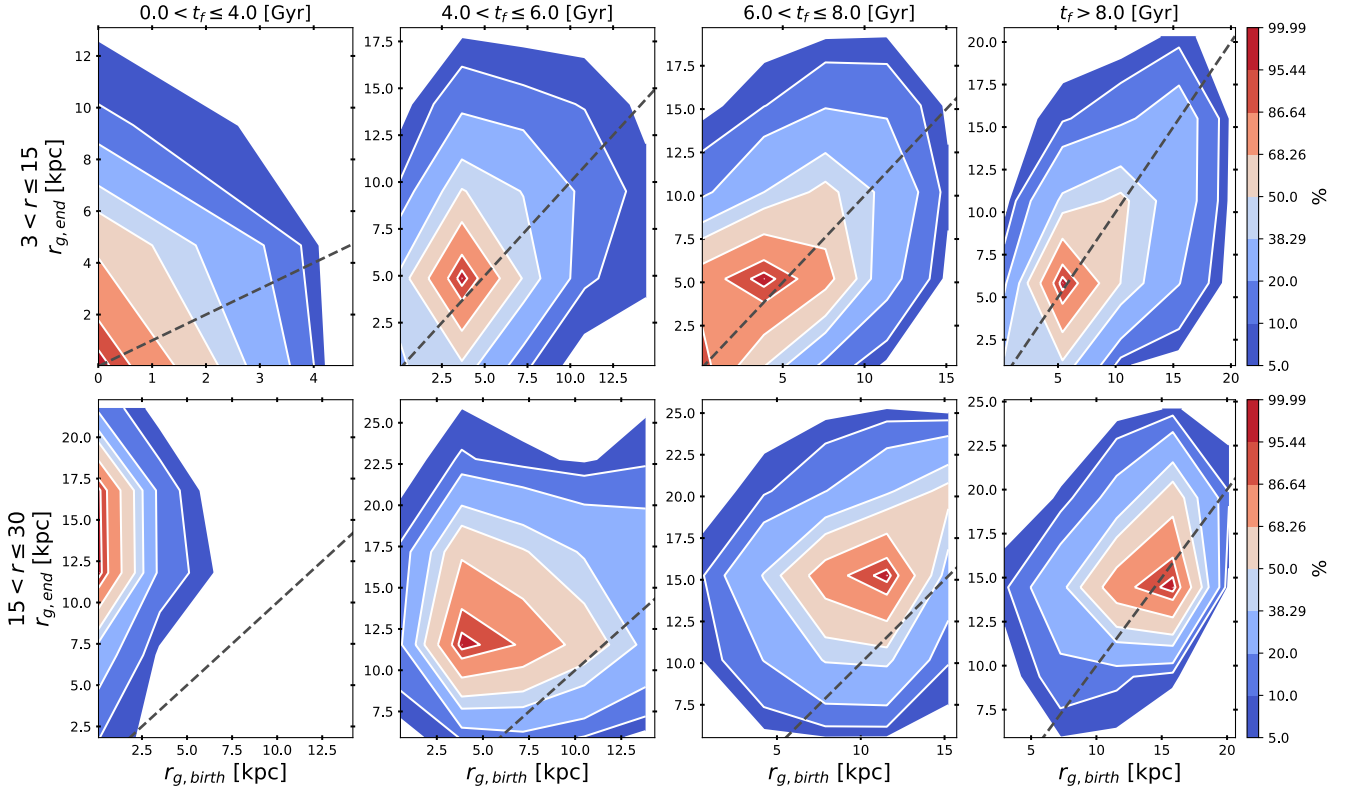


**Figure 12.** Stellar migration density probability, end guiding radius  $r_{g,end}$  versus birth guiding radius  $r_{g,birth}$  for in-situ star particles. *Top row:* stellar migration in the inner region,  $3 < r \leq 15$  kpc. *Bottom row:* stellar migration in the outer region,  $15 < r \leq 30$  kpc. The dashed line represents the locus of star particles for which no migration occurred. Old ( $t_f \leq 4$  Gyr) in-situ stars found at large radii ( $r \geq 15$  kpc) have migrated from the inner region towards the outskirts of M33.

$V_{los}$ , averaging to 0, i.e. implying radial orbits in the absence of angular momentum, and displaying a much higher dispersion,  $\sigma \sim 46$  km/s.

Future surveys will potentially be able to identify rotationally supported stars in the outskirts of M33, a signature that they are in-situ stars, and differentiate them from accreted ones. Our model predicts that the in-situ stellar population in the outskirts of the galaxy should have a flat radial age gradient as a result of accretion and stellar migration: in our particular simulation, the median stellar age of in-situ, co-rotating stars at large radii is 4–5 Gyrs. Accreted stars, on the contrary, are expected to be uniformly old, with a median age of  $\sim 11$  Gyrs.

## 4 CONCLUSIONS

We presented properties of a M33-analogue galaxy, simulated within the framework of Constrained Local Universe Simulations (Gottlöber et al. 2010; Di Cintio et al. 2012; Carlesi et al. 2016), run with the code GASOLINE (Wadsley et al. 2004a) and including supernova feedback à la Stinson et al. (2006), which allows for an efficient regulation of star formation within galaxies.

The properties of the simulated M33 are in fair agreement with observational data from Ferguson et al. (2007); Corbelli et al. (2014) and Kam et al. (2017), in terms of mass,

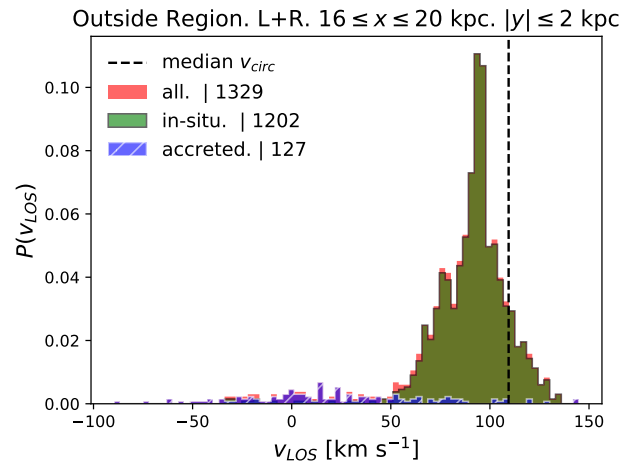


**Figure 13.** Line-of-sight velocity histograms of all (red), in-situ (green) and accreted (blue hatched fill) star particles, with the number of star particles in each category, within a  $4 \times 4$  kpc<sup>2</sup> region centered at the turnaround radius, after inclining the galaxy  $60^\circ$ , as the observed M33. The vertical dashed line is the galaxy’s circular velocity corrected for inclination. In-situ star particles co-rotate with the galactic disc, and lag with respect to the rotation curve due to the asymmetric drift effect, resulting from the non-zero stellar velocity dispersion. Accreted ones have a random distribution of their  $V_{los}$ , with a large dispersion.

rotation velocity, and surface brightness. Our simulated M33 has a total virial mass of  $2.7 \cdot 10^{11} M_{\odot}$  with a stellar mass of  $5.1 \cdot 10^9 M_{\odot}$ , placing the galaxy on the correct expectations from abundance matching prediction, a thin extended disc with scale length value of  $\sim 3.2$  kpc, and a rotation curve whose maximum value of  $V = 127.6$  km/s is reached at a radius of  $r \sim 17$  kpc, similar to what is reported in observations. The M33 simulated candidate does, however, have a small bulge in its inner region, not observed in the Triangulum galaxy: consequently we have avoided the region of the galaxy  $r < 3$  kpc in our analysis. In the CLUES-M33 analogue, we observe a trend of decreasing stellar age as we move towards outer radii, a sign of an inside-out formation of the disc (e.g. Pilkington et al. 2012), in which old stars are found within the inner most regions of a galaxy and young stars in the outskirts of the disc, as a result of newly accreting gas. In order to compare the observational results with our simulations we selected stellar particles within concentric annuli regions of similar thickness as the field of view of the HST/ACS camera, that has been used to derive the cumulative star formation history (SHF) of M33 along its major axis (Williams et al. 2009; Barker et al. 2011).

Interestingly, similarly to what was found in observations, the age gradient of stars in the simulated M33 shows a turnaround at large radii,  $r \geq 17$ -20 kpc, with the percentage of old stars ( $t_f < 4$  Gyrs) increasing from  $\sim 20$  to  $\sim 80$  per cent, moving from radii 14 to 30 kpc. Several proposals appear in the literature for explaining such age profile turnaround: stellar migration (Roškar et al. 2008a,b; Ruiz-Lara et al. 2016b), projection effects (Barker et al. 2011), a decrease in gas volume density possibly related to the warps in the disc (Sánchez-Blázquez et al. 2009), and accretion events from mergers (Gill et al. 2005; Sales et al. 2007; Brook et al. 2012; Ruiz-Lara et al. 2016b).

In this work, we demonstrate that this age reversal is mostly a result of accretion of old ( $t_f \leq 4$  Gyrs) stars from merging satellite galaxies into the main host galaxy and, to a much lesser extent, of stellar migration of old in-situ stars from the central regions towards the outskirts of M33. This result is in agreement with previous work by Ruiz-Lara et al. (2016b), using more massive galaxies. Indeed, at large radii where the age turnaround is found, about 93 per cent of the old stars come from accretion events, while only a mere 7 per cent were formed within the M33 galaxy disc (i.e. are in-situ): the reversal in the stellar age gradient disappears when considering only in-situ star particles. This suggests that accretion from mergers are the origin of the turnaround in our simulated M33.

This scenario could be verified observationally, studying the kinematic of stars in the outer fields of M33: in-situ stars should be co-rotating with the galactic disc, and should have a relatively small velocity dispersion  $\sigma$ , while accreted stars, which are kinematically hot, are expected to have a random distribution in their line-of-sight velocity, and to show a large velocity dispersions (in our model, more than two times higher than the  $\sigma$  of in-situ stars at the same radius). Moreover, the median age of the rotationally supported, in-situ stars, should indicate that this stellar population is young (median age of 4-5 Gyrs), unlike the pressure supported, accreted stars, causing the age turnaround, which should be all old (median age  $\sim 11$  Gyrs).

We highlight that the method used is sensitive to pro-

jection effects. While changing the inclination of the galaxy did not induce an apparent change in the turnaround radius region observed in the cumulative star formation history of the galaxy (i.e.  $17 \leq r \leq 20$  kpc), since it only provides a rough estimation of the turnaround radius; considering the correlation between the age reversal radius in the median formation time profile and the break radius of the surface brightness and stellar mass density profiles we are able to trace the projection effects through the break radius. Therefore, projection effects must be thought of carefully since they might play an important role in the determination of the true age turnaround radius.

Similar to what was found in observations (Ferguson et al. 2007), a break in the surface brightness profile of our M33 candidate in its inclined configuration appears at  $r = 17.6$  kpc (5.3 times its disc scale length), coinciding with the radius at which the age turnaround is found. Moreover, following the Martín-Navarro et al. (2012, 2014) classification, we detect a truncation coexisting with an up-bending of the surface brightness profile associated with the stellar halo component of the simulated galaxy at  $r = 25$  kpc. Similar results are obtained from the stellar surface mass density profile of the M33 candidate, i.e. a comparable disc scale length, and a break and a truncation at the same radii. Thus, both the radial mass distribution of the star particles and their age/metallicity contributes to the reversal of the age gradient at the outskirts of the galaxy. Recently, Ruiz-Lara et al. (2017) showed, using simulations, that breaks are a consequence of the combined effects of outward-moving and accreted stars, in good agreement with our results.

Finally, we note that Ruiz-Lara et al. (2016b) found similar results when studying Milky Way-mass galaxies in the RADES (RAMSES *Disc Environment Study* simulations, Few et al. 2012). In those simulations, the age reversal appears due to a combination of an inside-out growth of the disc, stellar migration (both inwards and outwards) of disc stars and accretion from old satellites: interestingly, as in our model, the age reversal was still recovered after suppressing stellar radial motion, indicating the minor relevance of stellar migration in generating the age upturn observed at large radii in massive galaxies.

In the future we intend to verify if the accretion phenomenon causing the age turnaround is dependent on the specific mass accretion history of each galaxy: in order to shed light on this we would need a large statistical sample of hydrodynamically simulated halos of M33's mass. The recently developed Local Group Factory (Carlesi et al. 2016) could be used to this aim.

## ACKNOWLEDGEMENTS

RM, AK, and CB are supported by the *Ministerio de Economía y Competitividad* and the *Fondo Europeo de Desarrollo Regional* (MINECO/FEDER, UE) in Spain through grant AYA2015-63810-P. ADC acknowledges financial support from the Karl-Schwarzschild fellowship program as well as a Marie-Sklodowska-Curie Individual Fellowship grant, H2020-MSCA-IF-2016 Grant agreement 748213 DIGESTIVO. AK is also supported by the Spanish Red Consolidar MultiDark FPA2017-90566-REDC and further thanks Jay-Jay Johanson for the long term physical effects. CB fur-

ther thanks the MICINN (Spain) for the financial support through the Ramon y Cajal programme. IM acknowledges support by the Deutsche Forschungsgemeinschaft under the grant MI 2009/1-1.

We would like to thank the anonymous referee for their very detailed and constructive comments that helped to improve the paper. We further thank Patricia Sánchez-Blázquez for valuable discussions.

This research has made use of NASA's Astrophysics Data System (ADS) and the arXiv preprint server.

## REFERENCES

- Bakos J., Trujillo I., Pohlen M., 2008, *ApJ*, **683**, L103
- Barker M. K., Ferguson A. M. N., Cole A. A., Ibata R., Irwin M., Lewis G. F., Smecker-Hane T. A., Tanvir N. R., 2011, *MNRAS*, **410**, 504
- Bensby T., Feltzing S., Oey M. S., 2014, *A&A*, **562**, A71
- Bird J. C., Kazantzidis S., Weinberg D. H., Guedes J., Callegari S., Mayer L., Madau P., 2013, *ApJ*, **773**, 43
- Brook C. B., Kawata D., Gibson B. K., Freeman K. C., 2004, *ApJ*, **612**, 894
- Brook C. B., et al., 2012, *MNRAS*, **426**, 690
- Bryan G. L., Norman M. L., 1998, *ApJ*, **495**, 80
- Burstein D., 1979, *ApJ*, **234**, 829
- Capaccioli M., 1989, in Corwin Jr. H. G., Bottinelli L., eds, *World of Galaxies (Le Monde des Galaxies)*. pp 208–227
- Carlesi E., et al., 2016, *MNRAS*, **458**, 900
- Chiappini C., Matteucci F., Gratton R., 1997, *ApJ*, **477**, 765
- Corbelli E., Schneider S. E., 1997, *ApJ*, **479**, 244
- Corbelli E., Thilker D., Zibetti S., Giovanardi C., Salucci P., 2014, *A&A*, **572**, A23
- Di Cintio A., Knebe A., Libeskind N. I., Hoffman Y., Yepes G., Gottlöber S., 2012, *MNRAS*, **423**, 1883
- Dolphin A. E., 2000, *PASP*, **112**, 1383
- Ferguson A., Irwin2 M., Chapman S., Ibata R., Lewis G., Tanvir N., 2007, *Astrophysics and Space Science Proceedings*, **3**, 239
- Few C. G., Gibson B. K., Courty S., Michel-Dansac L., Brook C. B., Stinson G. S., 2012, *A&A*, **547**, A63
- Fuhrmann K., 2008, *MNRAS*, **384**, 173
- Gill S. P. D., Knebe A., Gibson B. K., 2004, *MNRAS*, **351**, 399
- Gill S. P. D., Knebe A., Gibson B. K., 2005, *MNRAS*, **356**, 1327
- Gilmore G., Reid N., 1983, *MNRAS*, **202**, 1025
- Girardi L., et al., 2010, *ApJ*, **724**, 1030
- Gottlöber S., Hoffman Y., Yepes G., 2010, *Constrained Local UniversE Simulations (CLUES)*. Springer Berlin Heidelberg, Berlin, Heidelberg, pp 309–322, doi:10.1007/978-3-642-13872-0\_26, [http://dx.doi.org/10.1007/978-3-642-13872-0\\_26](http://dx.doi.org/10.1007/978-3-642-13872-0_26)
- Haywood M., Di Matteo P., Lehnert M. D., Katz D., Gómez A., 2013, *A&A*, **560**
- Hoffman Y., Ribak E., 1991, *ApJ*, **380**, L5
- Kam S. Z., Carignan C., Chemin L., Foster T., Elson E., Jarrett T. H., 2017, *AJ*, **154**, 41
- Karachentsev I. D., Karachentseva V. E., Huchtmeier W. K., Makarov D. I., 2004, *AJ*, **127**, 2031
- Katz N., Quinn T., Bertschinger E., Gelb J. M., 1994, *MNRAS*, **270**, L71
- Knollmann S. R., Knebe A., 2009, *ApJS*, **182**, 608
- Libeskind N. I., Hoffman Y., Tully R. B., Courtois H. M., Pomarède D., Gottlöber S., Steinmetz M., 2015, *MNRAS*, **452**, 1052
- Marigo P., Girardi L., Bressan A., Groenewegen M. A. T., Silva L., Granato G. L., 2008, *A&A*, **482**, 883
- Martín-Navarro I., et al., 2012, *MNRAS*, **427**, 1102
- Martín-Navarro I., Trujillo I., Knapen J. H., Bakos J., Fliri J., 2014, *MNRAS*, **441**, 2809
- Martínez-Serrano F. J., Serna A., Doménech-Moral M., Domínguez-Tenreiro R., 2009, *ApJ*, **705**, L133
- Minchev I., Chiappini C., Martig M., 2014, *A&A*, **572**, A92
- Minchev I., Martig M., Streich D., Scannapieco C., de Jong R. S., Steinmetz M., 2015, *ApJ*, **804**, L9
- Mo H. J., Mao S., White S. D. M., 1998, *MNRAS*, **295**, 319
- Moster B. P., Somerville R. S., Maulbetsch C., van den Bosch F. C., Macciò A. V., Naab T., Oser L., 2010, *ApJ*, **710**, 903
- Navarro J. F., White S. D. M., 1994, *MNRAS*, **267**, 401
- Patterson F. S., 1940, *Harvard College Observatory Bulletin*, **914**, 9
- Pérez E., et al., 2013, *ApJ*, **764**, L1
- Pilkington K., et al., 2012, *A&A*, **540**, A56
- Pontzen A., Roškar R., Stinson G., Woods R., 2013, pynbody: N-Body/SPH analysis for python, Astrophysics Source Code Library (ascl:1305.002)
- Reiprich T. H., Böhringer H., 2002, *ApJ*, **567**, 716
- Roškar R., Debattista V. P., Stinson G. S., Quinn T. R., Kaufmann T., Wadsley J., 2008a, *ApJ*, **675**, L65
- Roškar R., Debattista V. P., Quinn T. R., Stinson G. S., Wadsley J., 2008b, *ApJ*, **684**, L79
- Ruiz-Lara T., et al., 2016a, *MNRAS*, **456**, L35
- Ruiz-Lara T., Few C. G., Gibson B. K., Pérez I., Florido E., Minchev I., Sánchez-Blázquez P., 2016b, *A&A*, **586**, A112
- Ruiz-Lara T., Few C. G., Florido E., Gibson B. K., Pérez I., Sánchez-Blázquez P., 2017, *A&A*, **608**, A126
- Sales L. V., Navarro J. F., Abadi M. G., Steinmetz M., 2007, *MNRAS*, **379**, 1475
- Sánchez-Blázquez P., Courty S., Gibson B. K., Brook C. B., 2009, *MNRAS*, **398**, 591
- Sánchez-Blázquez P., et al., 2014, *A&A*, **570**, A6
- Santos-Santos I. M., Brook C. B., Stinson G., Di Cintio A., Wadsley J., Domínguez-Tenreiro R., Gottlöber S., Yepes G., 2016, *MNRAS*, **455**, 476
- Santos-Santos I. M. E., Domínguez-Tenreiro R., Granato G. L., Brook C. B., Obreja A., 2017, *A&A*, **603**, A4
- Sorce J. G., et al., 2016, *MNRAS*, **455**, 2078
- Spergel et al. D. N., 2007, *ApJS*, **170**, 377
- Srisawat C., et al., 2013, *MNRAS*, **436**, 150
- Stinson G., Seth A., Katz N., Wadsley J., Governato F., Quinn T., 2006, *MNRAS*, **373**, 1074
- Tacchella S., et al., 2015, *Science*, **348**, 314
- Tonry J. L., Dressler A., Blakeslee J. P., Ajhar E. A., Fletcher A. B., Luppino G. A., Metzger M. R., Moore C. B., 2001, *ApJ*, **546**, 681
- Verley S., Hunt L. K., Corbelli E., Giovanardi C., 2007, *A&A*, **476**, 1161
- Verley S., Corbelli E., Giovanardi C., Hunt L. K., 2009, *A&A*, **493**, 453
- Villalobos Á., Helmi A., 2008, *MNRAS*, **391**, 1806
- Wadsley J. W., Stadel J., Quinn T., 2004a, *New Astron.*, **9**, 137
- Wadsley J. W., Stadel J., Quinn T., 2004b, *New Astron.*, **9**, 137
- White S. D. M., Rees M. J., 1978, *MNRAS*, **183**, 341
- Williams B. F., Dalcanton J. J., Dolphin A. E., Holtzman J., Sarajedini A., 2009, *ApJ*, **695**, L15
- Willick J. A., Courteau S., Faber S. M., Burstein D., Dekel A., Strauss M. A., 1997, *ApJS*, **109**, 333
- Yoachim P., Dalcanton J. J., 2006, *AJ*, **131**, 226
- Yoachim P., Roškar R., Debattista V. P., 2012, *ApJ*, **752**, 97
- Zheng Z., et al., 2015, *ApJ*, **800**, 120

## APPENDIX A: DETERMINATION OF THE DISC SCALE LENGTH OF THE M33 CANDIDATE

To obtain luminosities from the simulation we used the routines available from PYNBODY. The code uses the Padova simple stellar populations (SSPs) isochrones and evolutionary tracks (Marigo et al. 2008; Girardi et al. 2010), with no dust extinction, to create a table which returns, for a set of ages and metallicities, a magnitude in the desired photometric system (see <http://stev.oapd.inaf.it/cgi-bin/cmd> for an overview of the different settings available for the table). PYNBODY reads the star particle's ages and metallicities returned from the simulation and interpolates the aforementioned table to associate magnitudes/luminosities to each star particle, and consequently, to the M33 candidate.

The  $i$ -band surface brightness profile has been fitted to a Sersic bulge and two exponential discs components corresponding to the inner and outer discs. Consequently, we used the following intensity profiles:

$$\begin{aligned} I_{\text{bulge}}(r) &= B_e \exp \left\{ -b_n \left[ (r/r_e)^{1/n} - 1 \right] \right\} \\ I_{\text{disc,in}}(r) &= D_{0,\text{in}} \exp \left\{ -(r/h_{\text{d,in}}) \right\} \\ I_{\text{disc,out}}(r) &= D_{0,\text{out}} \exp \left\{ -(r/h_{\text{d,out}}) \right\} \end{aligned} \quad (\text{A1})$$

where  $n$  is the Sersic index,  $b_n \approx 1.9992n - 0.3271$  (Capaccioli 1989 approximation),  $r_e$  the effective radius,  $h_d$  the disc scale length, and  $B_e, D_0$  the intensity at the effective radius and at  $r = 0$ , respectively. Thus, for the  $i$ -band, the surface brightness profile is:

$$\mu_i(r) = 25.73 - 2.5 \log_{10} I_i(r) \text{ mag arcs}^{-2} \quad (\text{A2})$$

where  $I(r)$  is expressed in  $L_{\odot} \text{ pc}^{-2}$ .

The fitting has been done in the following regions: the bulge,  $r \leq 2$  kpc; inner disc,  $5 \leq r \leq 14$  kpc; and outer disc,  $16.5 \leq r \leq 23$  kpc. These regions were chosen in order to avoid radial ranges where we see an overlap of galactic components, and to minimize contamination from old stars at the outskirts of the galaxy  $r \sim 30$  kpc. The same regions were used for the fit of the face-on view. The best-fit values for the inclined configuration are shown in Tab.A1.

To obtain the y-axis normalization value for the simulated profiles we used the inner disc fit models and best-fit parameters from Tab. A1, and linearly interpolated the curves at the desired radial value  $r = h_d$ . This has been done in order to avoid the contribution of the bulge when determining the normalization. On the other hand, since the observed M33 has no bulge component, we linearly interpolated the observational values directly at the (observational) disc scale length  $h_d^{\text{M33}} = 1.8$  kpc.

This paper has been typeset from a  $\text{\TeX}/\text{\LaTeX}$  file prepared by the author.

**Table A1.** Best-fit values for the surface brightness profile of the simulated M33 in the inclined configuration.

M33	$\mu_e(\mu_0)$ [mag arcs $^{-2}$ ]	$r_e(h_d)$ [kpc]	$n$
Bulge	$21.2 \pm 0.2$	$1.3 \pm 0.1$	$1.3 \pm 0.2$
Inner disc	$22.9 \pm 0.2$	$3.3 \pm 0.1$	-
Outer disc	$17.1 \pm 0.7$	$1.68 \pm 0.09$	-